



**HAL**  
open science

# Assessment of geometric nonlinearities influence on NASA rotor 37 response to blade tip/casing rubbing events

Elise Delhez, Florence Nyssen, Jean-Claude Golinval, Alain Batailly

► **To cite this version:**

Elise Delhez, Florence Nyssen, Jean-Claude Golinval, Alain Batailly. Assessment of geometric nonlinearities influence on NASA rotor 37 response to blade tip/casing rubbing events. ASME Turbo Expo 2021, Jun 2021, Virtual, United States. hal-03286204

**HAL Id: hal-03286204**

**<https://hal.science/hal-03286204>**

Submitted on 13 Jul 2021

**HAL** is a multi-disciplinary open access archive for the deposit and dissemination of scientific research documents, whether they are published or not. The documents may come from teaching and research institutions in France or abroad, or from public or private research centers.

L'archive ouverte pluridisciplinaire **HAL**, est destinée au dépôt et à la diffusion de documents scientifiques de niveau recherche, publiés ou non, émanant des établissements d'enseignement et de recherche français ou étrangers, des laboratoires publics ou privés.

## Assessment of geometric nonlinearities influence on NASA rotor 37 response to blade tip/casing rubbing events

Elise Delhez<sup>1,2</sup>, Florence Nyssen<sup>1</sup>, Jean-Claude Golinval<sup>2</sup>, Alain Batailly<sup>1</sup>

### Abstract

This paper uses a recently derived reduction procedure to study the contact interactions of an industrial blade undergoing large displacements. The reduction technique consists in projecting the dynamical problem onto a reduction basis composed of Craig-Bampton modes and a selection of their modal derivatives. The internal nonlinear forces due to large displacements are evaluated with the stiffness evaluation procedure and contact is numerically handled using Lagrange multipliers. The numerical strategy is applied on an open industrial compressor blade model based on the NASA rotor 37 blade in order to promote reproducibility of results. Two contact scenarios are investigated: one with direct contact between the blade and the casing and one with an abradable material deposited on the casing. The influence of geometric nonlinearities is assessed in both cases. In particular, contact interaction maps and abradable coating wear pattern maps are used to identify the main interactions that can be detrimental for the engine integrity.

### Keywords

Reduced order model, geometrical nonlinearities, rotor/stator interaction

1 - Department of Mechanical Engineering, Polytechnique Montréal, P.O. Box 6079, Succ. Centre-Ville, Montréal, Québec, Canada H3C 3A7  
2 - Department of Aerospace and Mechanical Engineering, University of Liège, allée de la Découverte 9, 4000 Liège, Belgium

## Évaluation de l'influence des non-linéarités géométriques sur la réponse du rotor 37 de la NASA à des interactions de contact aube/carter

Elise Delhez<sup>1,2</sup>, Florence Nyssen<sup>1</sup>, Jean-Claude Golinval<sup>2</sup>, Alain Batailly<sup>1</sup>

### Résumé

Dans cet article, une méthode de réduction récemment développée est utilisée pour étudier les interactions en contact d'une aube industrielle soumise à de grands déplacements. La méthode de réduction consiste à projeter le problème dynamique sur une base de réduction composée de modes de Craig-Bampton et d'une sélection de leurs dérivées modales. Les forces internes non linéaires causées par les grands déplacements de la structure sont évaluées avec la méthode dite 'stiffness evaluation procedure' et le contact est traité numériquement à l'aide de multiplicateurs de Lagrange. La stratégie numérique est appliquée à un modèle ouvert d'aube de compresseur industriel (l'aube rotor 37 de la NASA) afin de permettre la reproductibilité des résultats. Deux scénarios de contact sont étudiés, respectivement avec contact direct entre l'aube et le carter et avec un matériau abrasable déposé sur le carter. L'influence des non-linéarités géométriques est évaluée dans les deux cas. En particulier, des cartes d'interaction et des cartes d'usure sont utilisées pour identifier les interactions en contact les plus dangereuses pour l'intégrité du moteur.

### Mots-clés

Modèle réduit, non-linéarités géométriques, interaction rotor/stator

1 - Département de génie mécanique, Polytechnique Montréal, P.O. Box 6079, Succ. Centre-Ville, Montréal, Québec, Canada H3C 3A7  
2 - Département d'aérospatiale et mécanique, Université de Liège, allée de la Découverte 9, 4000 Liège, Belgique

## Introduction

In an increasingly competitive global market, aircraft engine manufacturers try to design more efficient engines in order to reduce their fuel consumption both for economic and environmental reasons. Over the past decade, different avenues have been considered to achieve this goal. First, aerodynamic losses can be decreased by reducing the clearance between the blades and the surrounding casing. This can lead to contact events between the blades and the casing even in nominal operating conditions [1, 2, 3]. In order to lower contact severity, an abradable coating acting as a sacrificial material is often deposited along the stator circumference [4, 5]. Also, the engine weight can be reduced by designing lighter, and therefore more flexible, blades. As a consequence, the blades can undergo large displacements and deformations [6, 7, 8]. The development of lighter and thinner blades by engine manufacturers, with reduced clearance between the rotating blades and the surrounding casing, asks for new design approaches. The large amplitude vibrations of these blades and their structural contact with the casing make indeed classical linear models unfit for the purpose.

Current industrial numerical models are characterized by a huge number of degrees-of-freedom and are not well suited for the study of nonlinear phenomena. Nonlinear reduced order models offer a promising alternative and receive therefore more and more attention in the academic world. Reduction by projection on a reduced space is often used in the literature because of its ease of implementation, but also because it keeps the general expression of the equation of motion so that the same integration algorithms as those used for the full order model can be used. Different reduction bases have been recently investigated in a nonlinear context by different authors: linear bases [9, 10], bases obtained from Proper Orthogonal Decomposition (POD) [11, 8], linear bases augmented with modal derivatives (MD) [12, 13, 14] and bases composed of nonlinear complex modes [15, 16].

Intrusive and non-intrusive methods have been derived to determine the nonlinear forces due to large displacements in the reduced space. In the case of intrusive methods, the reduced nonlinear forces are identified by direct projection of the full order nonlinear forces [17, 18, 19]. To the contrary, non-intrusive methods, which are advantageously compatible with commercial finite element software packages, rely on a polynomial expression of the reduced nonlinear forces, described as a function of the reduced coordinates whose coefficients are identified with nonlinear static evaluations [20, 21].

Different numerical strategies can be used to predict contact interactions with high fidelity finite element models, or, more efficiently, with reduced order models. Contact is usually numerically managed with penalty methods [22], with Lagrange multipliers [23] or with the augmented Lagrangian approach [24]. Because the stability of rubbing interactions is closely linked to nonlinear vibration modes, reduction bases have to intrinsically account for the nonlinear behavior of the blade [25].

When dealing with complex industrial systems featuring one or several nonlinear interfaces, existing reduction methods do not meet industrial needs, as they often consider only one type of nonlinearity or rely on over simplified assumptions. In this work, a new methodology, based on a reduction procedure, is used to study rubbing contact interactions of industrial compressor blades accounting for geometric nonlinearities. Particular attention is paid to the characterization of the contact stiffening phenomenon. The numerical strategy is applied on an open industrial compressor blade model, the NASA rotor 37 blade, in order to promote reproducibility of results. Two contact scenarios are investigated: one with direct contact between the blade and the casing and one with abradable material deposited on the casing.

The paper is organized as follows. First, the reduction procedure is described. The numerical strategy used for contact and wear treatment in the reduced space is also detailed. Then, a specific case study is presented with a description of the open blade model selected as well as the contact scenario. The reduction procedure is then applied to this blade model and the influence of geometric nonlinearities is assessed with in-depth analyses over a wide angular speed range.

## Methodology

The dynamics of mechanical structures is usually studied with high fidelity finite element models. The spatially discretized equation of motion governing the physical displacement  $\mathbf{u}$  of the structure around its equilibrium state

writes

$$\mathbf{M}\ddot{\mathbf{u}} + \mathbf{C}\dot{\mathbf{u}} + \mathbf{K}\mathbf{u} + \mathbf{g}_{nl}(\mathbf{u}) = \mathbf{f}_e(t) + \mathbf{f}_c(\mathbf{u}, \dot{\mathbf{u}}), \quad (1)$$

where  $\mathbf{M}$  is the mass matrix,  $\mathbf{C}$  is the viscous damping matrix,  $\mathbf{K}$  is the linear stiffness matrix,  $\mathbf{g}_{nl}(\mathbf{u})$  is the nonlinear internal forces vector,  $\mathbf{f}_e(t)$  is the external forces vector and  $\mathbf{f}_c(\mathbf{u}, \dot{\mathbf{u}})$  accounts for possible contact interactions. The time dependence of  $\mathbf{u}$  is omitted for clarity.

In this work, finite element models are reduced using the projection-based model order reduction technique introduced in [26]. The basic idea behind linear projection-based model order reduction techniques is to write the displacement field  $\mathbf{u}$  as a linear combination of spatial basis functions  $\Phi$

$$\mathbf{u}(t) = \Phi \mathbf{q}(t). \quad (2)$$

The physical displacement  $\mathbf{u} \in \mathbb{R}^N$  is therefore linearly reduced to a set of generalized coordinates  $\mathbf{q} \in \mathbb{R}^r$ , where  $r \leq N$  (in practice  $r \ll N$ ). In such reduction methods, the physical displacement vector  $\mathbf{u}$  can be partitioned into inner degrees-of-freedom,  $\mathbf{u}_i$ , that are effectively reduced and boundary degrees-of-freedom,  $\mathbf{u}_b$ , that are kept as physical degrees-of-freedom in the reduced space. The structural matrices  $\mathbf{M}$ ,  $\mathbf{C}$  and  $\mathbf{K}$  and the force vectors  $\mathbf{g}_{nl}$ ,  $\mathbf{f}_e$  and  $\mathbf{f}_c$  are partitioned accordingly with respect to inner (subscript  $i$ ) and boundary (subscript  $b$ ) degrees-of-freedom. The vector of generalized coordinates  $\mathbf{q}$  can therefore be written as

$$\mathbf{q} = \begin{bmatrix} \mathbf{u}_b \\ \boldsymbol{\eta} \end{bmatrix}, \quad (3)$$

where  $\boldsymbol{\eta}$  stands for modal generalized coordinates with no physical meaning. Keeping physical degrees-of-freedom among the generalized coordinates is for instance useful to allow the treatment of contact directly in the reduced space.

Injecting Eqn. (2) in Eqn. (1), the projection of the equation of motion in the reduced space writes

$$\tilde{\mathbf{M}}\ddot{\mathbf{q}} + \tilde{\mathbf{C}}\dot{\mathbf{q}} + \tilde{\mathbf{K}}\mathbf{q} + \tilde{\mathbf{g}}_{nl}(\mathbf{q}) = \tilde{\mathbf{f}}_e(t) + \tilde{\mathbf{f}}_c(\mathbf{q}, \dot{\mathbf{q}}), \quad (4)$$

where the projected matrices take the expressions

$$\tilde{\mathbf{M}} = \Phi^T \mathbf{M} \Phi, \quad \tilde{\mathbf{C}} = \Phi^T \mathbf{C} \Phi, \quad \tilde{\mathbf{K}} = \Phi^T \mathbf{K} \Phi \quad (5)$$

and the projected vectors are

$$\tilde{\mathbf{g}}_{nl}(\mathbf{q}) = \Phi^T \mathbf{g}_{nl}(\Phi \mathbf{q}), \quad \tilde{\mathbf{f}}_e = \Phi^T \mathbf{f}_e, \quad \tilde{\mathbf{f}}_c(\mathbf{q}, \dot{\mathbf{q}}) = \Phi^T \mathbf{f}_c(\Phi \mathbf{q}, \Phi \dot{\mathbf{q}}). \quad (6)$$

The numerical strategy used in this paper is adapted from an existing strategy that does not consider geometric nonlinearities in which the Craig-Bampton reduction method is combined with the Lagrange forward multiplier algorithm to study blade tip/casing contact interactions [27]. This reduction procedure has been validated against full order model data [28] and experimental data [29, 30]. The addition of geometric nonlinearities (through the addition of modal derivatives in the reduction basis and the use of the STEP to assess the nonlinear internal forces due to large displacements) has been studied in [26]. The following sections detail the features of the reduction procedure used in this work, *i.e.* the definition of the subspace  $\Phi$  on which the problem is projected, the way the projected nonlinear term  $\tilde{\mathbf{g}}_{nl}(\mathbf{q})$  is evaluated and the numerical strategy adopted for the treatment of contact in the reduced space.

In the present work, the core numerical tool is written in Python. The finite element software Samcef is used to perform the analyses with the full order finite element model required for building the reduced order model. The numerical strategy could be easily included in any commercial finite element software as it is non intrusive.

### Reduction basis

In this work, the reduction basis  $\Phi$  is composed of  $r$  Craig-Bampton modes [31] and a selection of  $r_{\text{MD}}$  modal derivatives [32, 33]. The Craig-Bampton modes consist in  $r_b$  constraint modes  $\Psi$  and  $r_c$  fixed interface linear normal modes  $\Theta$ .

The constraint modes, or Guyan modes, correspond to the linear static deformation of the structure to unit displacements at the boundary degrees-of-freedom  $\mathbf{u}_b$ . Adopting the degrees-of-freedom partitioning described above, they can be written as

$$\Psi = \begin{bmatrix} \Psi_i \\ \mathbf{I} \end{bmatrix}, \quad (7)$$

where  $\Psi_i$  is the solution of

$$\mathbf{K}\Psi = \begin{bmatrix} \mathbf{K}_{ii} & \mathbf{K}_{ib} \\ \mathbf{K}_{bi} & \mathbf{K}_{bb} \end{bmatrix} \begin{bmatrix} \Psi_i \\ \mathbf{I} \end{bmatrix} = \begin{bmatrix} \mathbf{0} \\ \mathbf{R} \end{bmatrix}, \quad (8)$$

which gives

$$\Psi_i = -\mathbf{K}_{ii}^{-1}\mathbf{K}_{ib}. \quad (9)$$

The fixed interface linear normal modes correspond to the modes of the structure clamped at the boundary interface degrees-of-freedom  $\mathbf{u}_b$ . They can be written as

$$\Theta = \begin{bmatrix} \Theta_{i,r_c} \\ \mathbf{0} \end{bmatrix}, \quad (10)$$

where  $\Theta_{i,r_c}$  is formed by truncating the solution  $\Theta_i$  of the eigenvalue problem

$$\mathbf{K}_{ii}\Theta_i = \mathbf{M}_{ii}\Theta_i\omega^2 \quad (11)$$

to the first  $r_c$  modes.

In order to account for the second-order effects that occur when considering geometric nonlinearities, the Craig-Bampton basis is here enriched with modal derivatives. Denoting by  $\tilde{\Phi}(\mathbf{u})$  the  $r$  Craig-Bampton modes ( $r_b$  constraint modes and  $r_c$  fixed interface linear normal modes) computed at a certain level of deformation  $\mathbf{u}$ , modal derivatives write

$$\xi_{jk} = \left. \frac{\partial \tilde{\phi}_j}{\partial q_k} \right|_{\mathbf{q}=\mathbf{0}} \quad j, k = 1, \dots, r, \quad (12)$$

where  $\tilde{\phi}_j$  stands for the  $j^{\text{th}}$  mode of the reduction basis  $\tilde{\Phi}$  and  $q_k$  is the  $k^{\text{th}}$  generalized coordinate, see Eqn. (2). In practice, the modes  $\tilde{\Phi}(\mathbf{u})$  are computed in the same way as the modes  $\Psi$  and  $\Theta$  in Eqn. (7) and Eqn. (10) by using the tangent stiffness matrix

$$\mathbf{K}_T = \mathbf{K} + \frac{\partial \mathbf{g}_{nl}}{\partial \mathbf{u}} \quad (13)$$

instead of the stiffness matrix  $\mathbf{K}$  in Eqn. (9) and Eqn. (11).

Different methods exist to compute these modal derivatives [34]. They are here computed by neglecting the inertial terms as suggested in [35, 34]. Modal derivatives are therefore computed by solving the linear systems

$$\mathbf{K}\psi_{jk} = - \left. \frac{\partial \mathbf{K}_T}{\partial q_j} \right|_{\mathbf{q}=\mathbf{0}} \phi_k. \quad (14)$$

The interface component of the modal derivatives is not null since the interface is not set fixed. Since the interface motion is already full represented by the constraint modes, the modal derivatives are modified to fixed interface modes by subtracting the component already present in the constraint modes

$$\begin{bmatrix} \zeta_{jk} \\ \mathbf{0} \end{bmatrix} = \begin{bmatrix} \xi_{jk,i} \\ \xi_{jk,b} \end{bmatrix} - \begin{bmatrix} \Psi_i \\ \mathbf{I} \end{bmatrix} \xi_{jk,b}. \quad (15)$$

It can be shown that modal derivatives are symmetric [12], *i.e.*

$$\zeta_{jk} = \zeta_{kj}, \quad (16)$$

so that a basis consisting in  $r$  linear modes can be enhanced with  $r(r+1)/2$  modal derivatives. The size of the reduction basis therefore increases quadratically with the number of Craig-Bampton modes. It is however expected that only a few modal derivatives are necessary to capture the nonlinear behavior of the structure [36]. In order to limit *a priori* the size of the reduction basis, a selection procedure is followed to determine which modal derivatives have to be included in the reduction basis to achieve accurate results. In this selection procedure, a weight is associated to all modal derivatives according to the interaction between the modes in a linear simulation and the modal derivatives characterized by the highest weights are selected. The weights are defined as

$$W_{jk} = \int_0^T |q_j(t)q_k(t)| dt, \quad (17)$$

where  $W_{jk}$  represents the weight associated to the modal derivative  $\zeta_{jk}$  and  $q_j(t)$  is the time varying amplitude of the  $j^{\text{th}}$  linear mode obtained in the linear response to a given applied external loading of duration  $T$ . This selection criterion based on the modal interaction between the modes has proven to be efficient to select modal derivatives [32, 26]. It should be noted that the selection procedure is not computationally expensive as it only involves a linear simulation of the system, *i.e.* a numerical time integration of Eqn. (1) where the nonlinear terms are neglected ( $\mathbf{g}_{nl}(\mathbf{u}) = \mathbf{0}$  and  $\mathbf{f}_c(\mathbf{u}, \dot{\mathbf{u}}) = \mathbf{0}$ ).

The augmented Craig-Bampton reduction basis and the associated reduction technique therefore write

$$\mathbf{u} = \Phi \mathbf{q} = \begin{bmatrix} \Psi_i & \Theta_{i,r_c} & \mathbf{Z} \\ \mathbf{I} & \mathbf{0} & \mathbf{0} \end{bmatrix} \begin{bmatrix} \mathbf{u}_b \\ \eta_c \\ \eta_{\text{MD}} \end{bmatrix}, \quad (18)$$

where the modal derivatives  $\zeta_{jk}$  are combined in  $\mathbf{Z}$  and  $\eta_c$  and  $\eta_{\text{MD}}$  are modal generalized coordinates corresponding to the fixed interface linear normal modes and the modal derivatives.

### Computation of the reduced nonlinear internal forces

The reduced nonlinear internal forces  $\tilde{\mathbf{g}}_{nl}(\mathbf{q})$  are evaluated with the STiffness Evaluation Procedure (STEP) [21]. This non-intrusive method is compatible with commercial finite element software packages and has proven to be efficient for the modeling of dynamical mechanical systems subjected to large displacements [21, 37, 9, 38]. This method consists in imposing static displacement fields and determining the corresponding internal nonlinear forces.

In the STEP, the nonlinear term  $\tilde{\mathbf{g}}_{nl}(\mathbf{q})$  is written as a third-degree polynomial in terms of the generalized coordinates  $q_i$ . Each component  $\tilde{g}_{nl}^m(\mathbf{q})$  of  $\tilde{\mathbf{g}}_{nl}(\mathbf{q})$  is therefore approximated by

$$\tilde{g}_{nl}^m(\mathbf{q}) = \sum_{i=1}^r \sum_{j=i}^r \tilde{A}_{ij}^m q_i q_j + \sum_{i=1}^r \sum_{j=i}^r \sum_{k=j}^r \tilde{B}_{ijk}^m q_i q_j q_k. \quad (19)$$

The identification of the third order tensor  $\tilde{\mathbf{A}}$  and the fourth order tensor  $\tilde{\mathbf{B}}$  requires  $(r^3 + 6r^2 + 5r)/6$  nonlinear forces static evaluations performed with the high fidelity finite element model with imposed displacements. The identification procedure is summarized in [21].

### Contact algorithm

Projection-based model order reduction techniques conserve the general form of the equation of motion (see Eqn. (1) and Eqn. (2)). Moreover the reduction procedure described above allows to retain physical degrees-of-freedom in the reduced space. Contact algorithms developed for full order finite element models can therefore be directly used for reduced models provided the boundary degrees-of-freedom  $\mathbf{u}_b$  include the contact interface.

The numerical strategy adopted here relies on the explicit central difference time integration scheme with the handling of contact using Lagrange multipliers, according to the Lagrange forward multiplier algorithm [23]. Such simulations in the time domain allow to capture the transient dynamics of the structure due to the occurrence of contact events. Friction is managed with the Coulomb law, under the assumption of sliding friction as the tangential speed to rotation is significantly larger than the vibration speed of the structure. The wear of the abradable coating is modeled by one-dimensional plastic compression [39]. The abradable coating is discretized with one-dimensional two-node rod elements independent from their adjacent neighbors and a linear isotropic hardening law is considered.

By noting  $\mathbf{q}_n$ , the numerical approximation of the exact value  $\mathbf{q}(t_n)$ , the classical explicit central finite difference scheme used in this work yields

$$\ddot{\mathbf{q}}_n = \frac{\mathbf{q}_{n+1} - 2\mathbf{q}_n + \mathbf{q}_{n-1}}{h^2} \quad \text{and} \quad \dot{\mathbf{q}}_n = \frac{\mathbf{q}_{n+1} - \mathbf{q}_{n-1}}{2h}, \quad (20)$$

where  $h$  is the time step of integration. At each time step  $t_{n+1} = t_n + h$ , the displacement field is first predicted without accounting for possible contact interaction as

$$\begin{aligned} \mathbf{q}_{n+1}^* = & \left( 2\tilde{\mathbf{M}} + h\tilde{\mathbf{C}} \right)^{-1} \left\{ 2h^2 \left[ \tilde{\mathbf{f}}_e(t_n) - \tilde{\mathbf{g}}_{nl}(\mathbf{q}_n) \right] \right. \\ & \left. + \left( 4\tilde{\mathbf{M}} - 2h^2\tilde{\mathbf{K}} \right) \mathbf{q}_n + \left( h\tilde{\mathbf{C}} - 2\tilde{\mathbf{M}} \right) \mathbf{q}_{n-1} \right\}. \end{aligned} \quad (21)$$

The predicted displacements are then used to evaluate the gap between the blade and the abradable coating and between the blade and the casing. If penetrations are detected between the impacting nodes and the abradable coating, the contact forces  $\tilde{\mathbf{f}}_{c,n+1}$  are computed through the use of massless compression elements with a piecewise linear plastic law as detailed in [39]. The abradable coating thickness is then locally reduced to account for abradable removal. If penetrations are detected between the blade and the rigid casing, the contact forces  $\tilde{\mathbf{f}}_{c,n+1}$  are computed in the normal and tangential directions through the use of Lagrange multipliers using the methodology described in [23] in order to cancel the penetrations of the impacting nodes. The contact forces are then used to correct the non-admissible displacements by

$$\mathbf{q}_{n+1} = \mathbf{q}_{n+1}^* + \left( \frac{\tilde{\mathbf{M}}}{h^2} + \frac{\tilde{\mathbf{C}}}{2h} \right)^{-1} \tilde{\mathbf{f}}_{c,n+1}. \quad (22)$$

### Case study

While obtaining relevant results for industrial mechanical systems calls for the use of realistic full 3D finite element models, the latter often prevent full disclosure of the results for confidentiality reasons. It is thus extremely arduous to compare existing numerical strategies dedicated to such analyses. The reduction procedure is here applied on an open industrial compressor blade model in order to promote reproducibility of results. The next two sections describe the blade model used throughout this article and the contact scenario to initiate contact interactions between the blade and the surrounding casing together with the parameters of the numerical simulations.

#### Open blade model

The test case consists in a single blade from the NASA rotor 37. NASA rotor 37 is a transonic axial flow compressor stage composed of 36 blades. It was initially designed and tested at NASA's Lewis Research Center in the late 70's [40, 41]. Since then, NASA rotor 37 has been often used as a benchmark to validate numerical methods in the fields of computational fluid dynamics [42]. The idea of using NASA rotor 37 as a benchmark in structural dynamics, and more specifically for contact simulations, has recently emerged [2, 26].

Rotor 37 is made of 200-grade maraging steel [41], a nickel alloy, with Young's modulus  $E = 180$  GPa, Poisson's ratio  $\nu = 0.3$  and density  $\rho = 8,000$  kg/m<sup>3</sup>. Each blade is characterized by a height of approximately 7 cm. The 3D geometry of the blade is here described with a finite element model with 20,657 nodes, *i.e.* 61,971 degrees-of-freedom (see Fig. 1). The compressor blade is clamped at its root. The first three eigenfrequencies of the blade are given by  $\omega_1 = 5,691.5$  rad/s,  $\omega_2 = 17,062.9$  rad/s and  $\omega_3 = 20,564.2$  rad/s. The associated linear mode shapes correspond respectively to the first bending (1B), first torsion (1T) and second bending (2B) modes. Modal damping coefficients  $\xi = 5 \cdot 10^{-4}$  for the first five modes and  $\xi = 5 \cdot 10^{-3}$  for the higher frequency modes are considered in the whole study.

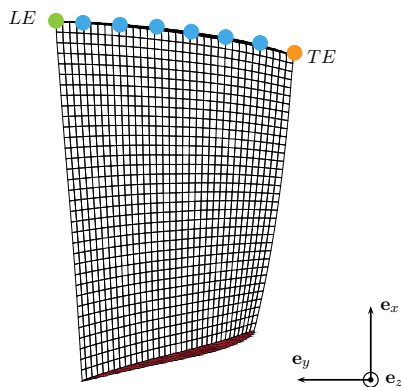


**Figure 1.** Finite element mesh of NASA rotor 37 blade, clamped surface (■) and 8 blade tip nodes (●) from leading edge (●) to trailing edge (●).

Possible penetrations and contact forces are computed at the 8 blade tip nodes – depicted in Fig. 1 – evenly distributed between the leading edge (node  $LE$ ) and the trailing edge (node  $TE$ ). The degrees-of-freedom of these 8 boundary nodes define the contact interface  $\mathbf{u}_b$  and are kept among the generalized coordinates  $\mathbf{q}$  (see Eqn. (3)). The reduced order model is built according to the methodology described above. The reduction basis is built by combining  $r_b = 24$  constraint modes (for the 8 boundary nodes),  $r_c = 20$  fixed interface linear normal modes and  $r_{MD} = 40$  modal derivatives, which leads to a reduced space size  $r = 84$ .

### Contact scenario

The blade is assumed to rotate at a constant speed  $\Omega$  about the  $\mathbf{e}_z$  axis. The blade is surrounded by a casing assumed to be infinitely rigid, *i.e.* insensitive to blade contact events. The casing follows the shape of the blade tip, so that the clearance  $c_0$  between the blade and the casing is uniform from the leading edge (node  $LE$ ) to the trailing edge (node  $TE$ ). As mentioned in the introduction, two contact scenarios are considered: one with direct contact between the blade and the casing, and one with an abradable coating deposited on the casing to mitigate contact interactions. For both direct contact and contact with abradable coating, friction is modeled using a Coulomb law, with a friction coefficient  $\mu = 0.15$ .

The abradable material is characterized by a Young's modulus  $E = 4$  GPa, a plastic modulus  $K = 1$  GPa and a yield stress  $\sigma_y = 1.5$  MPa, which is consistent with values encountered in the literature [5]. An abradable coating thickness of 5 mm is considered. The coating is modeled with 20,000 abradable elements distributed along the casing circumference.

At the beginning of the simulation, the casing is perfectly circular to avoid any initial penetration with a uniform operating clearance  $c_0$  from node  $LE$  to node  $TE$ . The clearance corresponds to the distance between the blade tip nodes and the abradable coating (or the casing in the absence of abradable coating) and is fixed to  $c_0 = 0.25$  mm. In order to initiate contact, the casing is progressively deformed in the radial direction until reaching the final

distortion

$$f(\theta) = h_b \exp \left[ - \left( \frac{\theta/\pi - \lfloor \theta/\pi \rfloor}{0.15} \right)^2 \right], \quad (23)$$

where  $\theta$  is the angular coordinate varying between 0 and  $2\pi$ . This distortion corresponds to an ovalization of the casing with the creation of two diametrically opposed bumps of height  $h_b$  corresponding to privileged contact areas (see Fig. 2). The height of the bumps is fixed to  $h_b = 0.5$  mm (twice the clearance). The response of the blade is computed by integrating the equation of motion (2) forward in time with a time step of integration  $h = 10^{-7}$  s.

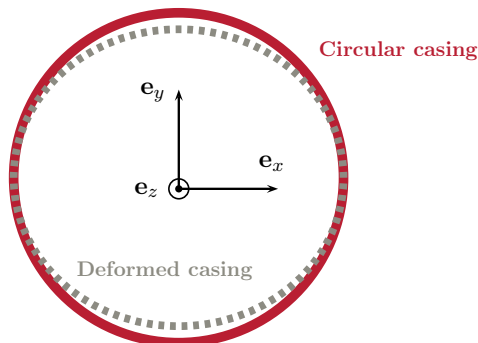


Figure 2. Progressive ovalization of the casing (not to scale).

The numerical convergence of the simulations with respect to the numerical scheme time step, the reduction parameters and the spatial discretization of the abradable coating has been checked carefully but is not detailed here for brevity.

## Results

The wide angular speed range from  $\Omega = 750$  rad/s to  $\Omega = 2,500$  rad/s is investigated for both considered contact scenarios. Each simulation is carried out at constant angular speed over 200 cycles of revolution.

### Direct blade/casing contact

In the first contact scenario, the rotating blade directly impacts the rigid surrounding casing. The blade tip radial displacement, directly related to the occurrence of contact events, is studied on the whole angular speed range. More precisely, the simulated radial displacement at the leading edge (node *LE* in Fig. 1) at each angular speed studied is analyzed in two steps. First, the overall displacement level is computed to obtain an indication of the criticality of the angular speed. The root-mean-square level of the radial displacement at *LE* is shown in Fig. 3 as a function of the angular speed in the cases where geometric nonlinearities are neglected (*i.e.* for  $\tilde{\mathbf{g}}_{nl}(\mathbf{q}) = \mathbf{0}$  in the equation of motion (2)) and where they are considered. Secondly, the frequency content of the radial displacement at node *LE* is computed at each angular speed on the second half of the time signal to get rid of transient effects. The corresponding interaction maps are plotted in Fig. 4(a) in the case where geometric nonlinearities are not considered and in Fig. 4(b) in the case where geometric nonlinearities are taken into account. Both maps have the same color scale from blue (lower amplitudes) to red (higher amplitudes).

As a first observation, it can be noted that taking into account the geometric nonlinearities reduces globally the amplitude of vibration on the whole angular speed range. This is patent in the RMS level figure (Fig. 3). In the same figure, it is also remarkable that both RMS signals look fundamentally different. The tangential response at *LE* (without geometric nonlinearities) is represented in Fig. 5 at three angular speeds – indicated by red markers (•) in Fig. 3 – corresponding to three different response levels. At  $\Omega = 1,500$  rad/s, the tangential response is below 3 mm and the geometrically linear and nonlinear response levels are very close. At  $\Omega = 1,700$  rad/s, the tangential

response reaches values close to 0.8 cm, greater than the tenth of the blade height, and the geometrically nonlinear effects start to be visible. At  $\Omega = 2,010$  rad/s, the tangential displacement is above 1.5 cm and the geometrically nonlinear regime is clearly reached. These differences in RMS levels show that geometric nonlinearities have a strong influence on blades contact dynamics, even for blades that are not particularly slender, such as compressor blades.

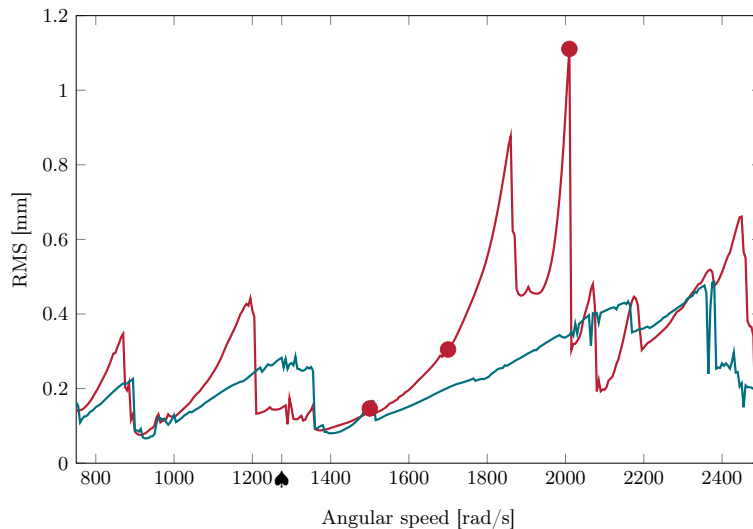
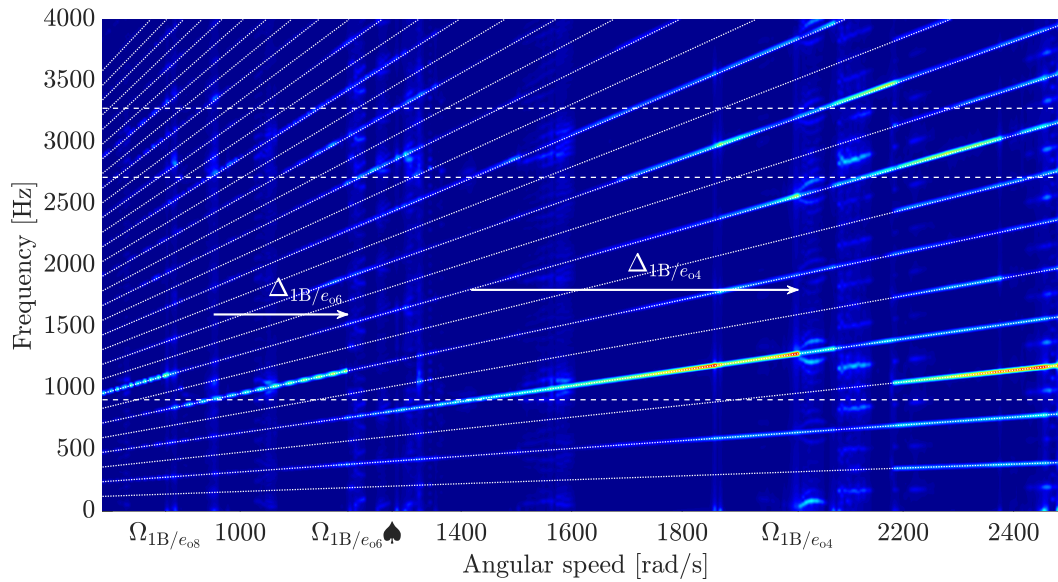


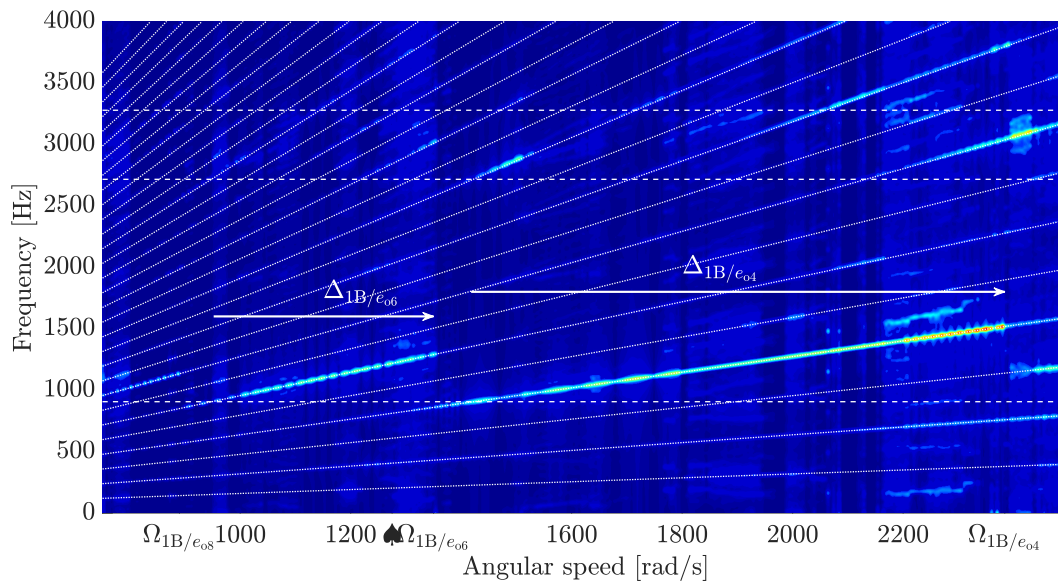
**Figure 3.** RMS levels of the radial displacement at *LE* for the case with direct contact (without geometric nonlinearities (—)) and with geometric nonlinearities (—).

Both interaction maps show lines of higher amplitudes on even engine order lines, which is consistent with the fact that the casing ovalization leads to an excitation occurring twice per revolution. For instance, at the angular speed  $\Omega = 1,350$  rad/s (indicated by the symbol ♠ in Fig. 3 and Fig. 4), the blade oscillates four times per cycle in the case where geometric nonlinearities are not considered and six times per cycle in the case where they are (see Fig. 6). Contributions of odd harmonics are also visible, particularly for the highest angular speeds studied. The steady-state response of the structure at  $\Omega = 2,450$  rad/s – represented in Fig. 7 – shows that the blade oscillates three times per cycle and only impacts one of the two bumps when geometric nonlinearities are not considered. The same observation holds for the case with geometric nonlinearities at higher angular speeds. Noninteger harmonics of the angular speed are also visible around 2,100 rad/s in Fig. 4(a) and around 1,800 rad/s in Fig. 4(b), which can be related to the nonlinear nature of the investigated system.

The interaction maps and the RMS level figures highlight the existence of contact interactions between the first vibration modes of the blade and even engine orders. These interactions are characterized by high amplitudes of vibration followed by amplitude jumps characteristic of nonlinear systems where the amplitude of the displacement suddenly drops for a small change of the angular speed. For the case where geometric nonlinearities are not considered, Fig. 4(a) shows the existence of interactions between the first bending mode and the engine orders 8, 6 and 4. These interactions are here denoted by  $1B/e_{o8}$ ,  $1B/e_{o6}$  and  $1B/e_{o4}$  and respectively occur at the angular speeds  $\Omega = 872$  rad/s,  $\Omega = 1,209$  rad/s and  $\Omega = 2,074$  rad/s. Because of contact stiffening, the angular speeds of the interactions are slightly higher than the angular speeds corresponding to the exact intersections between the first bending mode and the engine order lines. The increases in critical angular speeds due to contact stiffening are indicated in Fig. 4 by  $\Delta_{1B/e_{o6}}$  and  $\Delta_{1B/e_{o4}}$ . The contact stiffening leads to an increase of the first eigenfrequency from 906 Hz to respectively 1,161, 1,137 Hz and 1,297 Hz for the three interactions. The results in Fig. 4(b) also suggest that accounting for geometric nonlinearities yields a significant increase of contact stiffening. The interactions  $1B/e_{o8}$ ,  $1B/e_{o6}$  and  $1B/e_{o4}$  occur at higher angular speeds, respectively  $\Omega = 891$  rad/s,  $\Omega = 1,347$  rad/s and  $\Omega = 2,384$  rad/s. The blade stiffening due to the combined effect of contact and geometric nonlinearities leads to an increase of the first eigenfrequency from 906 Hz to respectively 1,175 Hz, 1,313 Hz and 1,489 Hz for the three interactions.



(a) Without geometric nonlinearities.



(b) With geometric nonlinearities.



**Figure 4.** Interaction maps of the radial displacement at *LE* for the case with direct contact (with eigenfrequencies (---) and engine order lines (·····)).

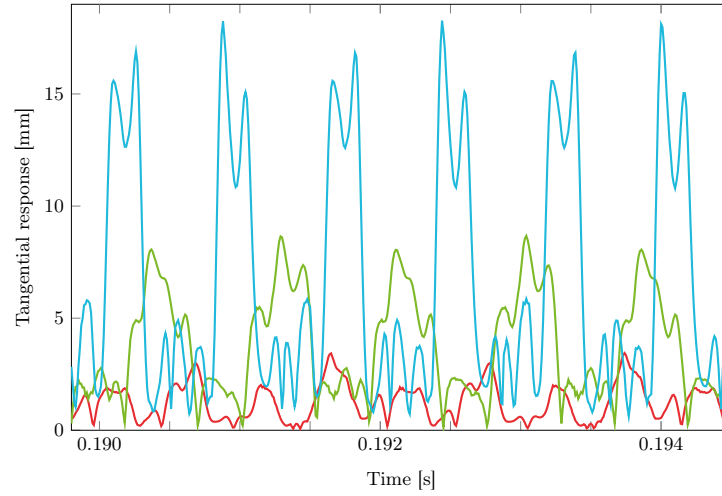


**Figure 5.** Tangential displacement at  $LE$  without geometric nonlinearities at  $\Omega = 1,500$  rad/s (—),  $\Omega = 1,700$  rad/s (—) and  $\Omega = 2,010$  rad/s (—).

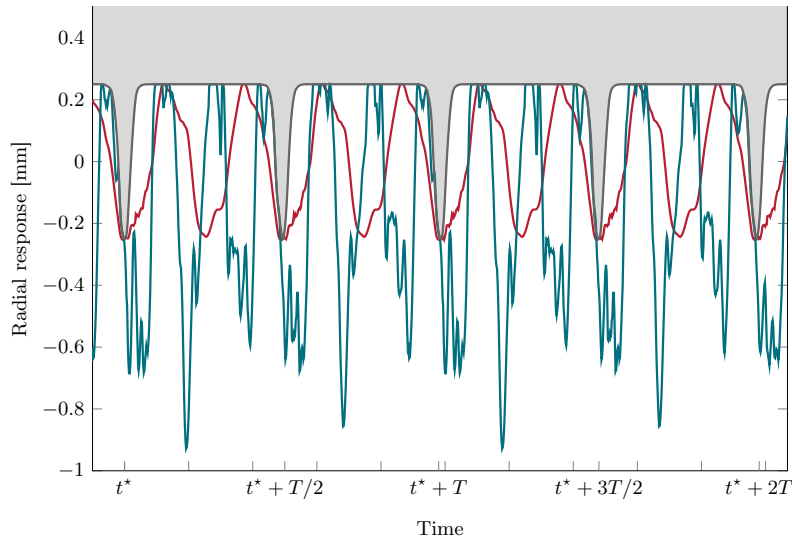


**Figure 6.** Radial displacement at  $LE$  at  $\Omega = 1,400$  rad/s (without geometric nonlinearities (—) and with geometric nonlinearities (—)) with rigid casing (■).

Some interactions with other vibration modes also lead to high amplitude displacements, such as interaction  $1T/e_{o12}$  occurring at  $\Omega = 1,497$  rad/s for the case without geometric nonlinearities and at  $\Omega = 1,509$  rad/s for the case with geometric nonlinearities .

#### Blade/casing contact with abradable coating

The blade tip radial displacement is then analyzed for the second contact scenario, with an abradable coating deposited on the casing. The corresponding RMS levels are represented in Fig. 8 in the cases where geometric nonlinearities are neglected and where they are considered and compared with the RMS levels obtained for the first contact scenario. The interaction maps are shown in Fig. 9 with the same color scale as in Fig. 4.

The wear level of the abradable coating along the circumference is also computed at the end of the simulations at each angular speed. The corresponding wear maps are given in Fig. 10. The two dark red lines that appear around

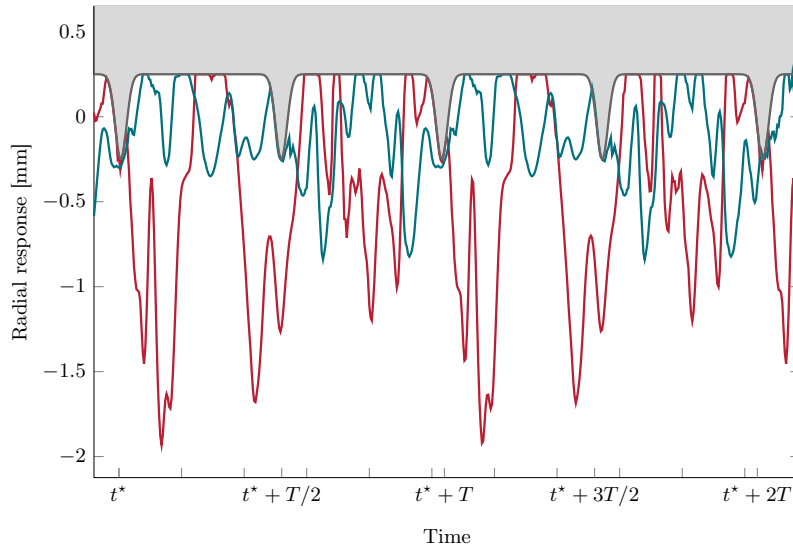


**Figure 7.** Radial displacement at  $LE$  at  $\Omega = 2,450$  rad/s (without geometric nonlinearities (—)) and with geometric nonlinearities (—)) with rigid casing (■).

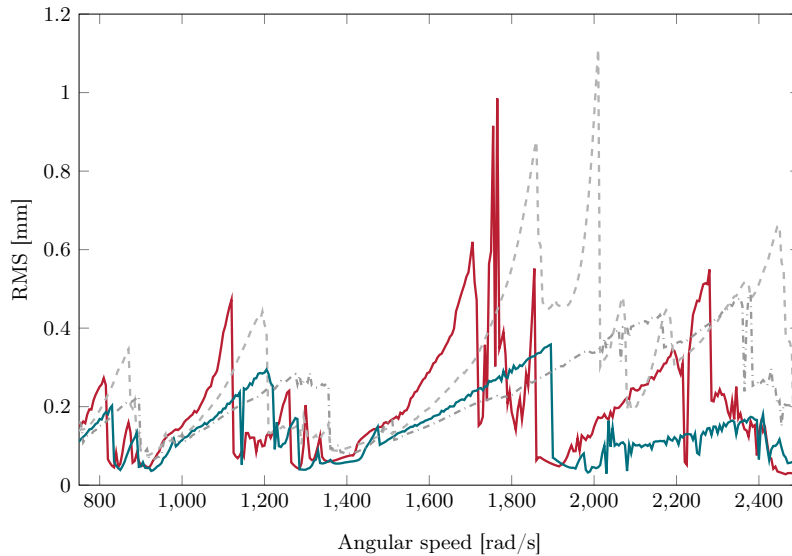
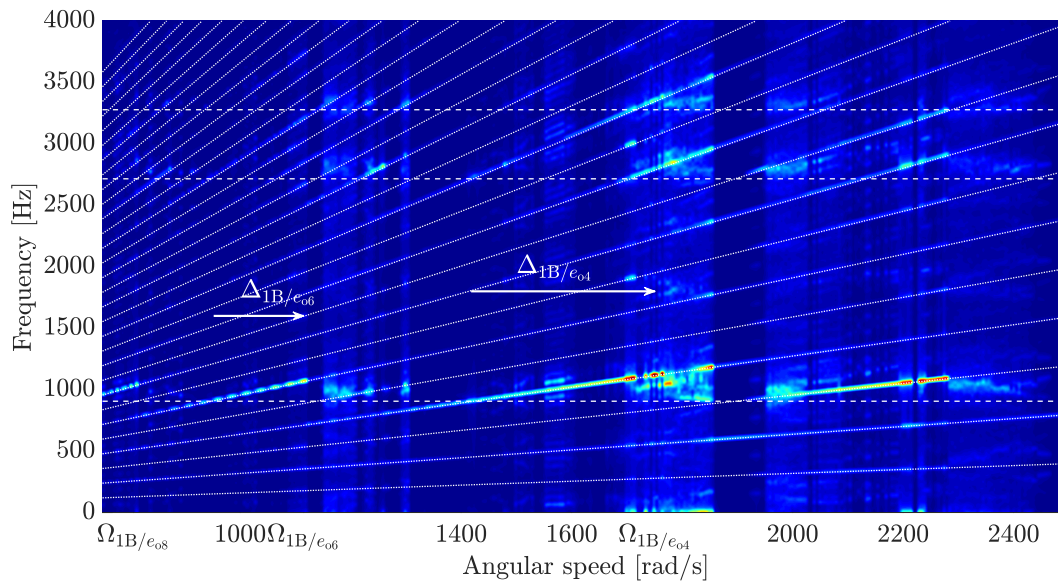


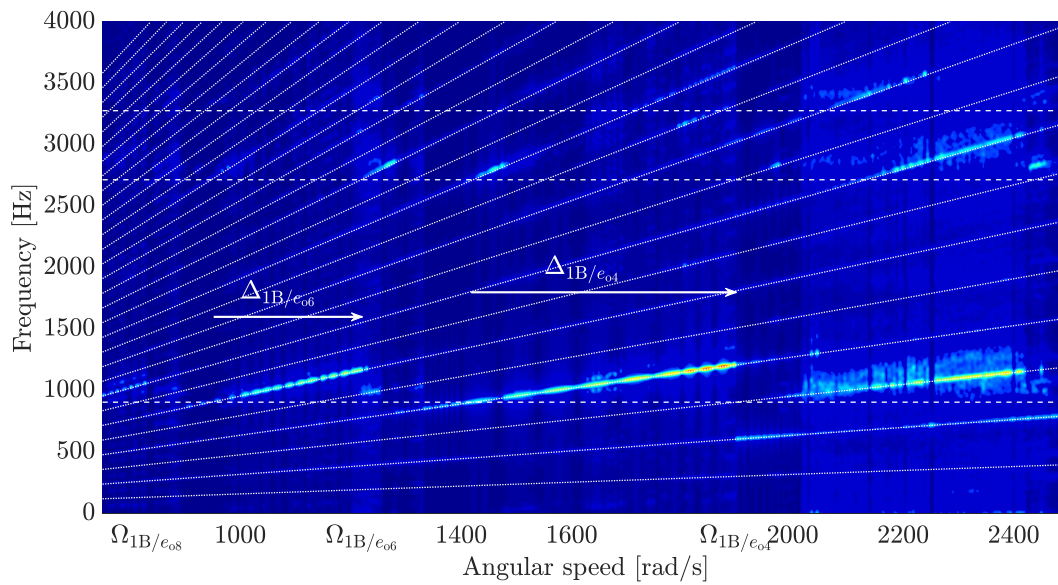
**Figure 8.** RMS levels of the radial displacement at  $LE$  for the case with abrasion coating (without geometric nonlinearities (—)) and with geometric nonlinearities (—)). In order to ease the comparison with Fig. 3, the RMS levels are also represented for the case with direct contact (without geometric nonlinearities (---)) and with geometric nonlinearities (-·-·).

$\theta = 1.5$  rad and  $\theta = 4.7$  rad correspond to the wear of the two bumps. The wear of the bumps occurs rapidly at the beginning of the simulation as shown in Fig. 11 which represents the evolution of the wear at node  $LE$  during the first 100 cycles of revolution at  $\Omega = 1,200$  rad/s (with geometric nonlinearities). The final level of wear of the abrasion coating between the lobes provides information on the type of interaction that occurred as deeper lobes are created at positions where the blade has impacted the casing repeatedly.

The RMS level figure, the interaction maps and the wear maps show that the abrasion coating acts as a sacrificial material and allows to mitigate contact severity. The results in Fig. 8 shows that the widths of the interactions are reduced compared to the first contact scenario: high displacement amplitudes are therefore reached on narrower



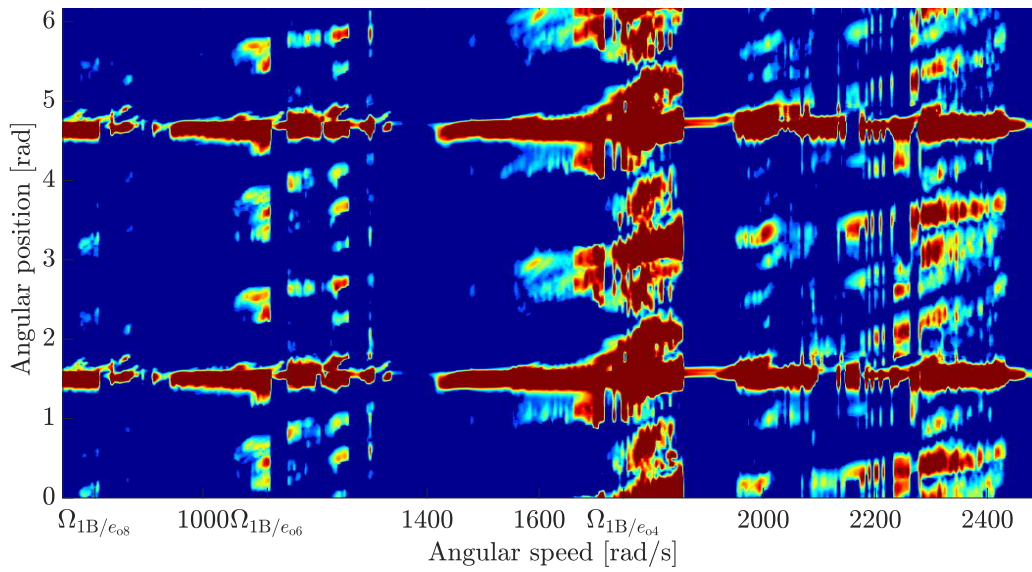
(a) Without geometric nonlinearities.



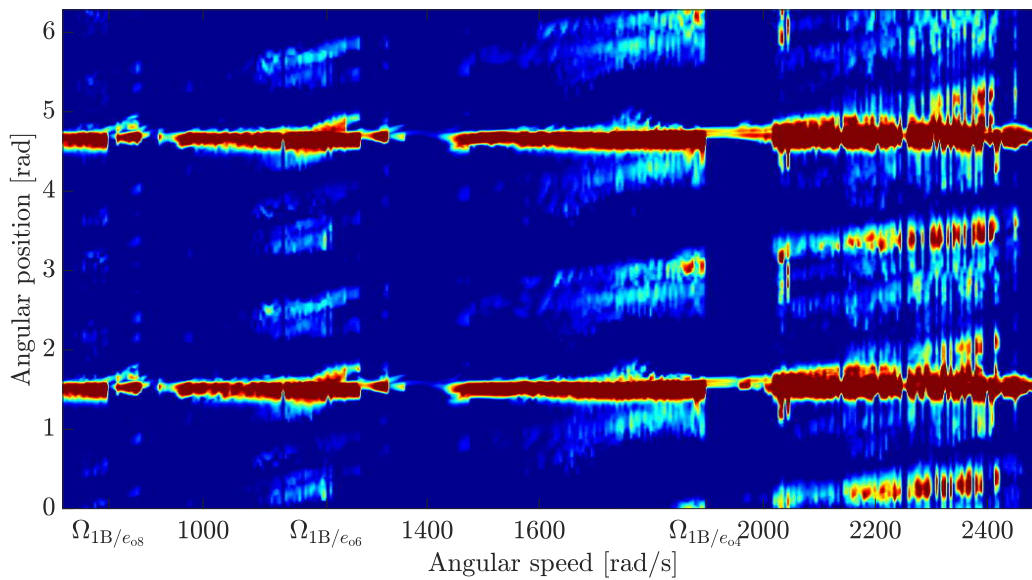
(b) With geometric nonlinearities.



**Figure 9.** Interaction maps of the radial displacement at *LE* for the case with abrasible coating (with eigenfrequencies (---) and engine order lines (·····)).



(a) Without geometric nonlinearities.



(b) With geometric nonlinearities.



Figure 10. Abradable coating wear maps at *LE* (at the end of the simulations).

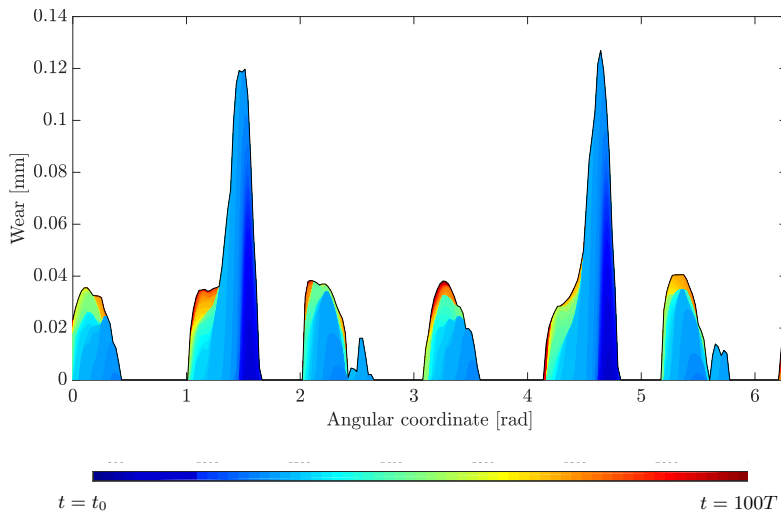


**Figure 11.** Evolution of the wear profile at *LE* during the first 100 cycles of revolution. Simulation at  $\Omega = 1,200$  rad/s with geometric nonlinearities.

angular speed intervals. The contact stiffening is also reduced compared to the case with direct contact between the blade and the casing. For the case without geometric nonlinearities, the interactions  $1B/e_{o8}$ ,  $1B/e_{o6}$ ,  $1B/e_{o4}$  now occur at the angular speeds  $\Omega = 815$  rad/s,  $\Omega = 1,124$  rad/s and  $\Omega = 1,765$  rad/s. Geometric nonlinearities are still responsible for an additional stiffening which is reduced compared to the scenario with direct contact between the blade and the casing. The interactions  $1B/e_{o8}$ ,  $1B/e_{o6}$ ,  $1B/e_{o4}$  occur at the angular speeds  $\Omega = 832$  rad/s,  $\Omega = 1,221$  rad/s and  $\Omega = 1,898$  rad/s. These interactions between the first bending mode and even engine order lines are clearly visible in the wear maps in Fig. 10 which shows the wear of 8, 6 or 4 lobes in the abradable coating at the angular speeds corresponding to the interactions.

The maps also highlight the existence of interactions with other vibration modes which lead to high amplitude displacements. In the case where geometric nonlinearities are not considered, the interaction  $1T/e_{o14}$  occurs at  $\Omega = 1,262$  rad/s and leads to the wear of 14 lobes in the abradable coating. Contact interactions with the first torsion mode are also visible in the case with geometric nonlinearities but are not strong enough to wear significantly the abradable coating. At  $\Omega = 1,470$  rad/s for instance, the nodes *LE* and *TE* vibrate in phase opposition (see Fig. 12), which confirms that this angular speed corresponds to the interaction  $1T/e_{o12}$ .

## Conclusion

In this article, a recently derived methodology has been used to study the rubbing contact interactions between a rotating blade and the surrounding casing. The methodology is based on a model order reduction procedure and allows to account for the geometrically nonlinear behavior of thin structures thanks to the enrichment of the Craig-Bampton reduction basis with modal derivatives and the use of the STEP to identify the nonlinear forces in the reduced space.

The methodology has been applied on a model of a compressor blade from the NASA rotor 37, which is an open blade model representative of industrial structures. Two contact scenarios have been investigated, one with direct contact between the rotating blade and the casing and one with an abradable coating deposited on the casing.

The comparison of the results without and with abradable coating show that the presence of an abradable coating allows to mitigate the contact interactions and to reduce the contact stiffening (both in the cases where geometric nonlinearities are considered and where they are not). The comparison of the results obtained without and with geometric nonlinearities shows that geometric nonlinearities have a strong influence on the contact dynamics of blades, even for blades that are not particularly thin and slender. In particular, geometric nonlinearities globally

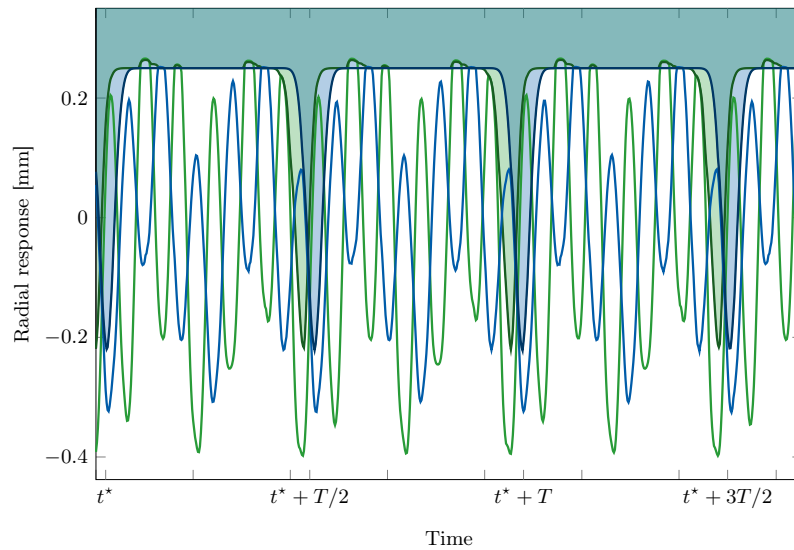


**Figure 12.** Radial displacement at *LE* (—) and *TE* (—) at  $\Omega = 1, 470$  rad/s (with geometric nonlinearities) with abradable coating at *LE* (■) and *TE* (■) .

reduce the amplitude of the vibration on the whole angular speed range studied and lead to an additional contact stiffening that must be considered to identify with accuracy the critical angular speeds of the engine.

It is expected that this numerical strategy could be used to improve the design of modern gas turbine engines. The low cost of the reduced order model simulations allows to perform systematic parametric studies in the preliminary design of engines. In particular, it could allow to account for nonlinear structural considerations from the beginning of the design process (in parallel to aerodynamic considerations), and therefore to accurately define the clearance between the blade tips and the casing.

As a next step, the reduction procedure will be adapted to full bladed disks with cyclic symmetry. Further developments will also include the introduction of uncertainties on the material and geometric parameters, known as mistuning, in the model.

## Acknowledgments

E. Delhez is supported by the *Fonds de la Recherche Scientifique* (F.R.S.-FNRS, Belgium) which is gratefully acknowledged. This research was also undertaken thanks to funding from the Canada Research Chairs Program.

## References

- [1] Sakulkaew, S., Tan, C. S., Donahoo, E., Cornelius, C., and Montgomery, M., 2013. “Compressor efficiency variation with rotor tip gap from vanishing to large clearance”. *Journal of Turbomachinery*, **135**(3). doi: 10.1115/1.4007547.
- [2] Piollet, E., Nyssen, F., and Batailly, A., 2019. “Blade/casing rubbing interactions in aircraft engines: Numerical benchmark and design guidelines based on NASA rotor 37”. *Journal of Sound and Vibration*, **460**, p. 114878. doi: 10.1016/j.jsv.2019.114878 - oai: hal-02281666.
- [3] Nyssen, F., Tableau, N., Lavazec, D., and Batailly, A., 2020. “Experimental and numerical characterization of a ceramic matrix composite shroud segment under impact loading”. *Journal of Sound and Vibration*, **467**, p. 115040. doi: 10.1016/j.jsv.2019.115040 - oai: hal-02378746.
- [4] Yi, M., He, J., Huang, B., and Zhou, H., 1999. “Friction and wear behaviour and abradability of abradable seal coating”. *Wear*, **231**(1), pp. 47–53. doi: 10.1016/S0043-1648(99)00093-9 - oai: hal-01555292.

- [5] Ma, X., and Matthews, A., 2007. “Investigation of abradable seal coating performance using scratch testing”. *Surface and Coatings Technology*, **202**(4-7), pp. 1214–1220. doi: 10.1016/j.surfcoat.2007.07.076 - oai: hal-01430526.
- [6] Vakakis, A. F., 1992. “Dynamics of a nonlinear periodic structure with cyclic symmetry”. *Acta Mechanica*, **95**(1-4), pp. 197–226. doi: 10.1007/BF01170813.
- [7] Grolet, A., and Thouverez, F., 2011. “Vibration Analysis of a Nonlinear System With Cyclic Symmetry”. *Journal of Engineering for Gas Turbines and Power*, **133**(2), p. 022502. doi: 10.1115/1.4001989 - oai: hal-01977265.
- [8] Picou, A., Capiez-Lernout, E., Soize, C., and Mbaye, M., 2019. “Mistuning analysis of a detuned bladed-disk with geometrical nonlinearities”. In Proceedings of the ASME Turbo Expo 2019. doi: 10.1115/GT2019-90820 - oai: hal-02175580.
- [9] Balmaseda, M., Jacquet-Richardet, G., Placzek, A., and Tran, D.-M., 2019. “Reduced order models for nonlinear dynamic analysis with application to a fan blade”. In Proceedings of ASME Turbo Expo 2019. doi: 10.1115/GT2019-90813 - oai: hal-02396583.
- [10] Di Palma, N., Martin, A., Thouverez, F., and Courtier, V., 2019. “Nonlinear Harmonic Analysis of a Blade Model Subjected To Large Geometrical Deflection and Internal Resonance”. In Proceedings of ASME Turbo Expo 2019. doi: 10.1115/GT2019-91213 - oai: hal-02159855.
- [11] Kerschen, G., Golinval, J.-C., Vakakis, A. F., and Bergman, L. A., 2005. “The method of proper orthogonal decomposition for dynamical characterization and order reduction of mechanical systems: An overview”. *Nonlinear Dynamics*, **41**(1-3), pp. 147–169. doi: 10.1007/s11071-005-2803-2.
- [12] Weeger, O., Wever, U., and Simeon, B., 2016. “On the use of modal derivatives for nonlinear model order reduction”. *International Journal for Numerical Methods in Engineering*, **108**, pp. 1579–1602. doi: 10.1002/nme.5267.
- [13] Wu, L., and Tiso, P., 2016. “Nonlinear model order reduction for flexible multibody dynamics: a modal derivatives approach”. *Multibody System Dynamics*, **36**(4), pp. 405–425. doi: 10.1007/s11044-015-9476-8.
- [14] Longobardi, P., 2019. *Model Order Reduction for Nonlinear Vibrations of Geometrically Nonlinear Structures*. Master thesis, Politecnico di Torino (Italy). URL: <https://webthesis.biblio.polito.it/11577/1/tesi.pdf>.
- [15] Joannin, C., Chouvion, B., Thouverez, F., Ousty, J.-P., and Mbaye, M., 2017. “A nonlinear component mode synthesis method for the computation of steady-state vibrations in non-conservative systems”. *Mechanical Systems and Signal Processing*, **83**, pp. 75–92. doi: 10.1016/j.ymsp.2016.05.044 - oai: hal-01389699.
- [16] Joannin, C., Thouverez, F., and Chouvion, B., 2018. “Reduced-order modelling using nonlinear modes and triple nonlinear modal synthesis”. *Computers and Structures*, **203**, pp. 18–33. doi: 10.1016/j.compstruc.2018.05.005 - oai: hal-01800394.
- [17] Capiez-Lernout, E., Soize, C., and Mignolet, M. P., 2012. “Computational stochastic statics of an uncertain curved structure with geometrical nonlinearity in three-dimensional elasticity”. *Computational Mechanics*, **49**(1), pp. 87–97. doi: 10.1007/s00466-011-0629-y - oai: hal-00684289.
- [18] Touzé, C., Vidrascu, M., and Chapelle, D., 2014. “Direct finite element computation of non-linear modal coupling coefficients for reduced-order shell models”. *Computational Mechanics*, **54**(2), pp. 567–580. doi: 10.1007/s00466-014-1006-4 - oai: hal-00955582.
- [19] Chaturantabut, S., and Sorensen, D. C., 2009. “Discrete Empirical Interpolation for Nonlinear Model Reduction”. In Proceedings of the 48th IEEE Conference, pp. 4316–4321. doi: 10.1109/CDC.2009.5400045.
- [20] McEwan, M. I., Wright, J. R., Cooper, J. E., and Leung, A. Y., 2001. “A combined modal/finite element analysis technique for the dynamic response of a non-linear beam to harmonic excitation”. *Journal of Sound and Vibration*, **243**(4), pp. 601–624. doi: 10.1006/jsvi.2000.3434.
- [21] Muravyov, A., and Rizzi, S., 2003. “Determination of nonlinear stiffness with application to random vibration of geometrically nonlinear structures”. *Computers and Structures*, **81**(15), pp. 1513–1523. doi: 10.1016/S0045-7949(03)00145-7.

- [22] Sinha, S. K., 2013. “Rotordynamic analysis of asymmetric turbofan rotor due to fan blade-loss event with contact-impact rub loads”. *Journal of Sound and Vibration*, **332**(9), pp. 2253–2283. doi: 10.1016/j.jsv.2012.11.033 - oai: hal-01555281.
- [23] Carpenter, N. J., Taylor, R. L., and Katona, M. G., 1991. “Lagrange constraints for transient finite element surface contact”. *International Journal for Numerical Methods in Engineering*, **32**(1), pp. 103–128. doi: 10.1002/nme.1620320107 - oai: hal-01389918.
- [24] Ma, H., Wang, D., Tai, X., and Wen, B., 2017. “Vibration response analysis of blade-disk dovetail structure under blade tip rubbing condition”. *Journal of Vibration and Control*, **23**(2), pp. 252–271. doi: 10.1177/1077546315575835.
- [25] Williams, R. J., 2011. “Simulation of blade casing interaction phenomena in gas turbines resulting from heavy tip rubs using an implicit time marching method”. In Proceedings of ASME Turbo Expo 2011. doi: 10.1115/GT2011-45495 - oai: hal-01555287.
- [26] Delhez, E., Nyssen, F., Golinval, J.-C., and Batailly, A., 2020. “Comparative study of blades reduced order models with geometrical nonlinearities and contact interfaces”. In Proceedings of ASME Turbo Expo 2020. doi: 10.1115/GT2020-14882 - oai: hal-02928234.
- [27] Batailly, A., Legrand, M., Cartraud, P., and Pierre, C., 2010. “Assessment of reduced models for the detection of modal interaction through rotor stator contacts”. *Journal of Sound and Vibration*, **329**(26), pp. 5546–5562. doi: 10.1016/j.jsv.2010.07.018 - oai: hal-00524762.
- [28] Legrand, M., Batailly, A., Magnain, B., Cartraud, P., and Pierre, C., 2012. “Full three-dimensional investigation of structural contact interactions in turbomachines”. *Journal of Sound and Vibration*, **331**(11), pp. 2578–2601. doi: 10.1016/j.jsv.2012.01.017 - oai: hal-00660863v3.
- [29] Batailly, A., Legrand, M., Millecamps, A., and Garcin, F., 2012. “Numerical-experimental comparison in the simulation of rotor/stator interaction through blade-tip/abradable coating contact”. *Journal of Engineering for Gas Turbines and Power*, **134**(8). doi: 10.1016/j.jsv.2012.01.017 - oai: hal-00746632.
- [30] Batailly, A., Agrapart, Q., Millecamps, A., and Brunel, J.-F., 2016. “Experimental and numerical simulation of a rotor/stator interaction event localized on a single blade within an industrial high-pressure compressor”. *Journal of Sound and Vibration*, **375**, pp. 308–331. doi: 10.1016/j.jsv.2016.03.016 - oai: hal-01333888.
- [31] Craig, R. R., and Bampton, M., 1968. “Coupling of substructures for dynamic analyses”. *AIAA Journal*, **6**(7), pp. 1313–1319. doi: 10.2514/3.4741 - oai: hal-01537654.
- [32] Tiso, P., 2011. “Optimal second order reduction basis selection for nonlinear transient analysis”. In Proceedings of the International Modal Analysis Conference (IMAC) XXIX, pp. 27–39. doi: 10.1007/978-1-4419-9299-4\_3.
- [33] Wu, L., Tiso, P., and van Keulen, F., 2016. “A modal derivatives enhanced Craig-Bampton method for geometrically nonlinear structural dynamics”. In Proceedings of the 27th International Conference on Noise and Vibration Engineering, pp. 3615–3624.
- [34] Slaats, P., de Jongh, J., and Sauren, A., 1995. “Model reduction tools for nonlinear structural dynamics”. *Computers & Structures*, **54**(6), pp. 1155–1171. doi: 10.1016/0045-7949(94)00389-K.
- [35] Idelsohn, S. R., and Cardona, A., 1985. “A reduction method for nonlinear structural dynamic analysis”. *Computer Methods in Applied Mechanics and Engineering*, **49**(3), pp. 253–279. doi: 10.1016/0045-7825(85)90125-2.
- [36] Tiso, P., 2011. “Effective modal derivatives based reduction method for geometrically nonlinear structures”. In Proceedings of ASME 2011 International Design Engineering Technical Conferences & Computers and Information in Engineering Conference (IDETC/CIE 2011), pp. 399–406. doi: 10.1115/DETC2011-48315.
- [37] Capiez-Lernout, E., Soize, C., and Mbaye, M., 2014. “Geometric nonlinear dynamic analysis of uncertain structures with cyclic symmetry. Application to a mistuned industrial bladed disk”. In Proceedings of the 26th International Conference on Noise and Vibration Engineering, pp. 4481–4494. oai: hal-01066543.

- [38] Givois, A., Grolet, A., Thomas, O., and Deü, J. F., 2019. “On the frequency response computation of geometrically nonlinear flat structures using reduced-order finite element models”. *Nonlinear Dynamics*, **97**, pp. 1747–1781. doi: 10.1007/s11071-019-05021-6 - oai: hal-02289755.
- [39] Legrand, M., Batailly, A., and Pierre, C., 2012. “Numerical investigation of abradable coating removal in aircraft engines through plastic constitutive law”. *Journal of Computational and Nonlinear Dynamics*, **7**(1), pp. 1–11. doi: 10.1115/1.4004951 - oai: hal-00627526.
- [40] Moore, R. D., and Reid, L., 1980. Performance of Single-Stage Axial-Flow Transonic Compressor With Rotor and Stator Aspect Ratios of 1.19 and 1.26, Respectively, and With Design Pressure Ratio of 2.05. Tech. rep., NASA TP 1659. URL: <https://ntrs.nasa.gov/citations/19790001889>.
- [41] Reid, L., and Moore, R. D., 1978. Design and Overall Performance of Four Highly-Loaded, High Speed Inlet Stages for an Advanced High-Pressure Ratio Core Compressor. Tech. rep., NASA TP 1337. URL: <https://ntrs.nasa.gov/citations/19780025165>.
- [42] Denton, J. D., 1997. “Lessons from Rotor 37”. *Journal of Thermal Science*, **6**(1). doi: 10.1007/s11630-997-0010-9.